EUROPEAN ORGANIZATION FOR NUCLEAR RESEARCH

CERN-EP/80-115
27 June 1980

THE ČERENKOV RING-IMAGING DETECTOR: RECENT PROGRESS AND FUTURE DEVELOPMENT

T. Ekelöf*), J. Séguinot**), J. Tocqueville†)

and T. Ypsilantis††)

Paper submitted to the
International Conference on Experimentation at LEP,
Uppsala, 16-20 June 1980.

---

*) CERN, Geneva, Switzerland.
**) Université de Caen, France.
†) Collège de France, Paris, France.
††) Ecole Polytechnique, Palaiseau, France.

THE ČERENKOV RING-IMAGING DETECTOR: RECENT PROGRESS AND FUTURE DEVELOPMENT

T. Ekelöf, CERN, European Organization for Nuclear Research, Geneva, Switzerland
J. Séguinot, Université de Caen, France
J. Tocqueville, Collège de France, Paris, France
T. Ypsilantis, Ecole Polytechnique, Palaiseau, France

Abstract

Results are reported on measurements of Čerenkov ring images using a multistage MWPC with an argon-TEA gas mixture. A specific detector response of $N_0 = 56\ cm^{-1}$ was obtained. It is shown that with some minor modifications to the detector, this value can be raised to $N_0 = 90\ cm^{-1}$. Using an argon-methane-TEA mixture in the MWPC, it is shown that efficient single-photoelectron detection can be achieved with proportional wire amplification without preamplification. A design of a new type of drift chamber (TPC) detector for two-dimensional measurement of the ring image is described. The use of the Čerenkov ring-imaging technique in high-energy physics experimentation is discussed, and in particular a full solid-angle detector for LEP is suggested.

1. Introduction

During the last few years, substantial progress [1-6] has been made by several groups towards the realization of Čerenkov ring-imaging detectors for use in high-energy physics experiments. In this paper we report on some recent progress made in measurements at the CERN Proton Synchrotron (PS) in January 1980. A multiwire proportional chamber (MWPC) with one-dimensional read-out was used for the photon detection. The gas filling used in the MWPC was argon or a mixture of argon and methane. In both cases a small admixture of triethylamine (TEA) was used as photosensitive gas component. Other such components with photoionization thresholds lower than that of TEA are briefly discussed.

To achieve two-dimensional read-out of the ring image, a time projection chamber (TPC) type drift chamber has been constructed, and tests of this chamber are currently in preparation.

In the last section we mention various features of the ring-imaging technique, making comparisons with the Čerenkov threshold detection technique. Possible applications of ring-imaging detectors in high-energy physics experiments are also discussed. In particular we suggest a full solid-angle ring-imaging detector for LEP, based on the drift chamber prototype described above. Some suggestions for intermediate developments of detectors covering a limited solid angle are also made.

2. Measurements using argon-TEA in the MWPC

The experimental layout used for these measurements is shown in Fig. 1 and is similar to that in the previous experiment of Séguinot

et al. [6]. Čerenkov radiation, produced by a 10 GeV/c pion passing through 1 m pure (1 ppm) argon gas at near atmospheric pressure, was focused by the spherical mirror onto the detector plane. The resulting ring image was observed by the photon detector shown in Fig. 2. It is composed of a CaF_2 window and three plane-parallel gaps (C, PA, and T) followed by a MWPC having a ±3.5 mm gap and 2 mm wire spacing. The diameter of the active area of the detector is 100 mm. The operating electric fields in the C, PA, and T gaps were 1.7, 7.6, and 1.4 kV/cm, respectively, in a direction such that electron drift occurs from C to PA to T to PC. The C gap serves to convert the incident photons to photoelectrons (by photoionization of TEA) which are transferred to the PA gap. This transfer is efficient owing to the large ratio of the electric fields E_{PA}/E_C. An electron entering the PA gap gets multiplied in this high-field region [7] and is transferred to gap T with a combined gain and transfer efficiency of G_{PA}. Subsequent transfer from T to PC occurs followed by avalanche multiplication around a 20 μm diameter wire of the proportional chamber with gain G_{PC}. The measured gains G_{PA} and G_{PC} versus applied potential are shown in Fig. 3. The presence of counting plateaus in PA and PC, shown in Fig. 4, demonstrates that efficient single-photoelectron counting occurs. The ordinate of Fig. 4 is n_{pe}, the average number of photoelectrons per incident pion, as defined below.

We observed an average of about three photoelectrons (n_{pe}) for each incident 10 GeV/c pion traversing 1 m of argon gas at 1.2 for absolute pressure. The value n_{pe} is defined in such a way that two or more contiguous hit wires contribute to n_{pe} as a single photoelectron. This is necessary because an electron swarm leaving gap

PA, due to a single photoelectron in gap C, can straddle several proportional chamber wire cells causing neighbouring wires to fire. The probability of two or more adjacent wires being fired by one photoelectron -- called the smearing probability -- has been measured [6] to between 30% and 50%, depending on TEA partial pressure and the PA gap electric field. Using different concentrations of TEA, we observed an average number of hit wires per event n_w which varied between 4.5 and 6, whereas the number of photoelectrons n_{pe}, as determined from the data, has a constant value of about three. The distributions of n_w and n_{pe}, for 10^4 incident pions, are shown in Fig. 5.

The ring image, as observed in projection by the one-dimensional (x) proportional chamber detector, has a density distribution [6]

$$\frac{dP}{dx} = \frac{1}{\pi} \frac{1}{\sqrt{r^2 - (x-x_c)^2}} , \qquad (1)$$

where r is the ring radius, and x_c the x component of the ring centre. Integrating this distribution over x from $x_i-(s/2)$ to $x_i+(s/2)$, around the i^{th} wire of the proportional chamber of wire spacing s, we find the probability P_i that a single incident photon will be detected by the i^{th} wire to be

$$P_i = \frac{1}{\pi}\left\{\sin^{-1}\left[\frac{x_i-x_c+(s/2)}{r}\right] - \sin^{-1}\left[\frac{x_i-x_c-(s/2)}{r}\right]\right\} . \qquad (2)$$

The experimental determination of P_i is feasible only as an average $\bar{P}_i$ over many incident particles having a mean angular beam aperture of half-angle α. In Fig. 6 we show the observed number of photoelectrons $n_{pe}(x)$ versus wire position x for $M = 10^4$ incident 10 GeV/c

pions. The plotted histogram is the best fit of $n \cdot M \cdot \bar{P}_i$ to $n_{pe}(x)$ obtained by varying the parameters n, r, x_c, and α. The fitted values are n = 2.85, r = 26.04 mm, x_c = -6.59 mm, and α = ±2.5 mrad.

There is a finite probability that two converted photons will fall on nearby wires or wire clusters, thereby getting counted as a single converted photon. This probability is a function of the smearing probability, as well as the circle radius r and the true number N of photoelectrons per event. The relation between N and the observed average number $n(\approx n_{pe})$ of photoelectrons per event was obtained by a Monte Carlo simulation for various assumed values of N and for the fixed values r = 27 mm, x_c = 6 mm, and α = ±1.25 mrad, and three values of the smearing probability, 0%, 30%, and 60%. The result is shown in Fig. 7. A value of n = 2.85 can be seen to correspond to N = 3.8.

The specific detector response N_0 is obtained from the equation [6]

$$N_0 = N \frac{f^2 + r^2}{Lr^2} , \tag{3}$$

where f is the mirror focal length, which is equal in our geometry to the radiator length L. Hence for N = 3.8, f = L = 1000 mm, and r = 26.0 mm, we find N_0 = 56.3 cm^{-1}.

The detector used has a 200 μm gap between the CaF_2 crystal and the first high-voltage mesh V_1 defining the start of the C-gap. Photons absorbed in this gap are not transferred to the C-gap and are therefore lost. At 20 Torr partial pressure of TEA, the 8.5 eV photon mean free path is 1.0 mm, hence the fraction of incident UV

photons lost in this gap was 18%. This loss can be recovered by vacuum deposition of the first mesh V_1 onto the CaF_2 window. An additional advantage is that 95% optical transparency may be obtained by this technique, compared to the present value of 81%. The total gain obtained in this way would be a factor of 1.43.

The transmission of 8.5 eV photons in the Čerenkov radiator gas was measured using a Kr gas scintillation light-source and was found to be 90% for an average Čerenkov photon path length of 1.5 m. It would be quite feasible to improve this transmission to 99% by more complete degassing of the stainless-steel vessel housing the radiator gas. These two modifications taken together would lead to an expected gain of 1.59 which, when applied to the present detector, would increase the value of N_0 from 56.3 cm^{-1} to 90 cm^{-1}. The transmission T of the 5 mm thick CaF_2 crystal and the reflectivity R of the f = = 1000 mm spherical mirror have been measured and are shown in Fig. 8. The values achieved, of about R = 75% and T = 68% at 8.5 eV, are reasonable and not much gain should be expected from mirror or crystal improvements. Also shown in Fig. 8 is the relative TEA quantum efficiency Q/Q_{max}, and the product QRT/Q_{max} = Total versus photon energy.

3. Measurements using argon-methane TEA in the MWPC

In this phase of the experiment we attempted to count single photoelectrons in mixtures of argon + methane + TEA without gain in gap PA but simple transfer from C through PA and T to PC with all the gain occurring in PC. The first set of measurements was performed with a gas mixture of 80% Ar and 20% CH_4, with 8 Torr TEA partial pressure. At this TEA concentration, the 8.5 eV photon mean free

path is 2.5 mm. With the electric fields in C, PA, and T set at 0.6, 1.25, and 2.50 kV/cm, we varied the electric field in PC to obtain the first plateau curve shown in Fig. 9 and labelled 20% CH_4. As is seen, the value of n_{pe} on plateau is about 2, rather than the previously obtained value of 3. We attribute this loss to the photon absorption in CH_4. In Fig. 10 the TEA relative quantum efficiency curve Q/Q_{max} is shown versus photon energy, with a dashed curve showing the methane absorption probability versus photon energy. Assuming that methane absorbs all the photons above 8.6 eV, a 33% loss in n_{pe} from 3 to 2 is obtained. This is shown in Fig. 9, where the horizontal dotted lines labelled E_2 = 8.7 eV and E_2 = 8.6 eV indicate the expected number of photoelectrons n_{pe} if methane photon absorption sets in above energy E_2.

The second and third plateau curves shown in Fig. 9 and labelled 50% CH_4 and 100% CH_4, show good counting efficiency but additional decrease of n_{pe} to 1.8 and then to 1.5. These additional losses of 0.9 and 0.75 are explained by the increase in TEA partial pressure from 8 Torr to 20 Torr and then to 40 Torr. At these partial pressures the photon mean free paths are 2.5 mm, 1.0 mm, and 0.5 mm and the corresponding loss factors in the 200 μm gap are 0.89 and 0.73, which is consistent with our observations.

In conclusion, the rightmost plateau curves of Fig. 9 show that efficient single-photoelectron counting in pure methane has been achieved with proportional wire amplification without preamplification. It follows from the earlier discussion that the N_0 value attainable with TEA in pure methane would be $N_0 = 60\ cm^{-1}$.

6. Drift detector (TPC) and two-dimensional ring image

Based on the experimental results of the previous sections, where efficient single-photoelectron counting is demonstrated, we propose to measure the full two-dimensional ring image with the drift detector shown schematically in Fig. 11. An applied electric field, parallel to the detector window, causes the produced photoelectrons to drift a maximum distance of 10 cm to a picket fence of proportional counter wires, as indicated in Fig. 11. The drift time τ gives the x coordinate of the photoelectron, and the wire address gives the y coordinate. In methane, the drift velocity is 1 mm in 12 ns. A chamber gas-filling of pure methane with 4 Torr TEA (photon mean free path of 5 mm) will require about a 20 mm thick drift gap for full (98%) photon absorption.

The diffusion coefficient in pure methane is small and corresponds to σ_x = 500 μm (or σ_τ = 6 ns) for an average drift distance of 5 cm. As electron diffusion is about five times greater in argon than in methane, the use of pure methane is thus essential for this application. To obtain equivalent resolution in the x and the y directions (i.e. $\sigma_y \approx \sigma_x$) will require a wire spacing of about 2 mm, hence 500 wires per metre, for a slab 10 cm across. For 1 m^2 of detector surface, 5000 drift wires with TAC read-out (having 6 ns time resolution) will thus be required.

A test detector, shown in Fig. 12, has been constructed, and initial tests of this detector are currently in preparation.

Recently some interesting new photoionizing gases have been proposed for photon detection, such as TMBI [8,9] and TMAE [8]. These

molecules both have the very low photoionization threshold of 5.4 eV, making possible the use of fused quartz windows. In Fig. 13 is shown the measured transmission of an 8 mm thick fused quartz window (Corning 7940) plotted together with the measured relative quantum efficiencies of TMBI and TMAE arbitrarily normalized to 50% at 7.2 eV. These curves show that the combination of, in the first place, TMBI, but also of TMAE, with fused quartz could be most interesting if the quantum efficiency will be shown to be high. The TMBI and TMAE vapour pressures are reported [8] as 0.1 and 0.2 Torr at 20 °C, which could correspond to absorption mean free paths of about 30 and 15 mm. If we require the photon absorption in a 20 mm thick drift gap to be of the order of 98%, the absorption mean free path should be about 5 mm. This can be obtained by raising the vapour pressure of the TMBI or the TMAE, by increasing the temperature to some 50 °C or 60 °C, implying a heated-counter operation.

5. Comparison of the method of Čerenkov ring-imaging detection with that of Čerenkov threshold detection

The detectors currently used for identification of π's, K's and p's above 1 GeV in high-energy physics experiments are the Čerenkov threshold detector and the specific ionization (dE/dx) detector. Of these, only the threshold can be used in the region 50-75 GeV/c and above. At high energies, both methods in general require measurements to be performed over many metres of particle track. This poses problems in experiments where large-angle apertures should be covered as, for example, in storage ring experiments. A method proposed to reduce the length of the dE/dx counter is to pressurize the gas. However, at present it is not clear whether this method will prove to work in practice, as expected.

Below we make a comparison of the Čerenkov ring-imaging method with the most commonly used of the two methods mentioned above, i.e. the Čerenkov threshold method.

A ring-imaging detector measures the angle θ of emission of the Čerenkov photons ($\theta = r/f$), the direction of motion of the radiating particle (from the position of the centre of the circle), and the number of emitted photons. It thus extracts far more information from the Čerenkov radiation than does the conventional threshold Čerenkov counter, which merely detects whether there is Čerenkov radiation emitted or not. Below we discuss the various advantages that the detailed information given by the ring imaging entails.

5.1 Measurement range and accuracy

A threshold Čerenkov counter will only indicate whether the velocity γ of the detected particle is above or below the threshold velocity γ_t of the counter. In some counters the pulse height from the photomultiplier is recorded, giving also some measure of γ in a limited range above γ_t. The accuracy in this measurement of γ is, however, strongly limited owing to the statistical fluctuations in the number N of photoelectrons. For high values of γ_t this number is low for a given radiator length L.

$$N^{\infty} = N_0 L/\gamma_t^2 \ , \qquad (4)$$

where N^{∞} is the asymptotic ($\gamma \to \infty$) number of photoelectrons and N_0 is the earlier-mentioned specific detector response parameter. From Eq. (4) is seen that one must accept low values of N^{∞} if γ_t is large and L cannot be increased.

The accuracy in the γ determination obtained from the same limited number of photoelectrons using the ring-imaging method is far larger, as the fluctuations in the emission angle θ of the Čerenkov photons are only due to the relatively small dispersion of the radiator refractive index n. In most practical cases these angular fluctuations are of the order of 1%, whereas the statistical fluctuations in N for, say, N = 10, are of the order of 30%. The relative importance of these fluctuations in θ and N at different values of γ can be seen in Fig. 14, where θ and N, both normalized to their asymptotic values θ^{∞} and N^{∞}, have been plotted versus γ normalized to γ_t [10]. Figure 15, where $1 - \theta/\theta^{\infty}$ has been plotted versus γ/γ_t shows in detail how θ approaches its asymptotic value θ^{∞} at large γ. From these plots, which are generally valid for gaseous radiators [i.e. for $(n-1) \ll 1$], it can be seen that if the radius r of the ring image ($r \approx f \cdot \theta$) can be measured to an accuracy of 1% this means that γ can be measured in the region from γ_t up to about $7\gamma_t$ (see Fig. 15). The corresponding upper limit when detecting the pulse height in threshold counters is situated below $2\gamma_t$ [$1.8\ \gamma_t$ for 30% fluctuations in n (see Fig. 14)].

Combining a ring-imaging detector with a magnetic spectrometer with a resolution $\Delta p/p \lesssim 10\%$ enables the identification of π's, K's and p's for γ values in the range γ_t up to the order $7\gamma_t$.

As can be seen from Fig. 15 the upper limit $7\gamma_t$ depends critically on the accuracy in the θ determination. This accuracy is not only related to the dispersion in the refractive index n but also to the spatial accuracy of the photon detector and to the number of photons detected, and is therefore different from one detector to

another. The value $7\gamma_t$ is therefore only given here to indicate a typical value of the upper limit for $\pi/K/p$ separation.

In a more limited range above γ_t the variation of θ with γ is strong (see Fig. 14), and a precise determination of γ from θ is possible. Up to the order of $2\gamma_t$ or $3\gamma_t$ the standard error in this determination is a few percent at most, given that θ is measured with a precision of about 1%. In this restrained γ range, the accuracy of the complementary magnetic spectrometer need only be of the order of $\Delta p/p \simeq 20\%$ for full particle separation. A precise value of the momentum p of each particle can then be obtained from the measured value of γ.

5.2 Granularity

In situations where many secondary particles should be identified using the threshold Čerenkov technique, the counter must be divided into many cells, each with a separate photomultiplier, so that the probability of having light from more than one particle going into one cell is small. The required number of cells can in practical cases be very large. In some situations the requirement can even be impossible to fulfil; namely, when the radiating particles emerge so close to each other that their Čerenkov radiation cones mix.

In a Čerenkov ring-imaging detector the granularity is determined by the two-photon separation of the photon detector and is of the order of millimetres. This means that the Čerenkov light from two particles can be measured separately even if the two Čerenkov light-cones mix and result in overlapping ring images. This feature

of the ring-imaging detector is particularly valuable when one wants to identify all particles in jets originating from quarks or gluons.

5.3 Compactness and solid angle

To make $\pi/K/p$ separation possible over a certain range in velocity γ covered by a given ring-imaging detector, a set of several threshold counters with different radiators is needed. As each of these counters in general should have a γ_t higher than that of the ring-imaging detector to bridge the region from γ_t to $\sim 7\gamma_t$, each of the threshold counters in the set should also be longer than the single ring-image counter [see Eq. (4)]. A ring-imaging detector will thus in general be far more compact than a set of threshold counters having the same possibilities of $\pi/K/p$ separation. This is an important advantage in any experimental set-up, fixed-target or storage ring, but particularly so in the latter case where solid angles up to 4π need to be covered.

6. Potential applications of the ring-imaging technique in high-energy physics experiments, in particular at LEP

From the discussion in the preceding section, it follows that the ring-imaging technique could be favourably used to substitute the threshold technique in most cases where the latter is employed in fixed-target or storage ring experiments. The gain would be in terms of accuracy, range of γ measurement, geometrical compactness, and relaxed requirements on the accuracy of the momentum determination.

The application of the method should be adjusted to the needs in each particular case. In most fixed-target experiments the solid angle to be covered is only a small part of 4π, and the secondary particles can be made to pass a magnetic spectrometer in series with

the Čerenkov ring detector, thereby making identification over a wide range in γ (from γ_t to $\sim 7\gamma_t$) possible. Examples of experimental set-ups of this kind are the EMC spectrometer, the NA3 set-up and the Omega spectrometer at CERN, and the E605 experiment at Fermilab.

The same application of the technique can also be used in such storage ring detectors where only a limited solid angle is covered by Čerenkov counters. The TASSO detector at PETRA is an example of such a set-up. In this case the three radiators used in threshold mode could be replaced by one liquid-nitrogen radiator used for ring imaging with a great gain in compactness (the whole counter would be reduced in length from about 3 m to some 40 cm, making possible the use of calorimeters also behind the Čerenkov arms).

Other more restrictive applications of the method may be thought of. For example, if one uses a simple photon detector of less accurate spatial resolution than that assumed above, the range of measurement and resolution in γ will decrease but the granularity of the counter may still be quite high.

The first application of the method in a particle physics experiment will most probably be a case in which only a limited solid angle need be covered. However, it is in experiments at large storage rings such as LEP, and in which a 4π solid angle should be covered, that all the potentialities of the method can be exploited. In Fig. 16 we show a pentagon-shaped detector module, made up of five triangular TPC-type detectors. Twelve such modules combine to form a dodecahedron covering the full solid angle, as shown in Fig. 17.

The module shown in Fig. 17 has a liquid Ne radiator for measurement of low-energy particles ($1.4 < \gamma < 21.5$). Two additional counters, one with xenon gas and the other with an argon + neon gas mixture (both at atmospheric pressure) as radiators, can be used in cascade outside the liquid Ne detector to cover a γ range up to about 200 ($26 < \gamma < 63$ for Xe and $60 < \gamma < 195$ for Ar+Ne). The outer "radii" of the three concentric dodecahedrons is 0.75, 1.5, and 3.0 m, and the whole assembly will thus approximate a sphere of 6 m diameter. Within the range of γ given for each of the three detectors, the calculated resolution is $\Delta\gamma/\gamma \lesssim 4\%$. This detector thus needs to be complemented with a spectrometer measuring the particle momenta with a resolution of only $\Delta p/p \sim 20\%$. This could be achieved with a small magnetic spectrometer ($B \approx 0.2$ T) housed in the spherical volume, of diameter 1 m, inside the inner liquid Ne detector. The stray field of the magnet must be small enough not to curve the tracks significantly within the radiator regions.

The set-up should furthermore be complemented with electromagnetic (and perhaps hadronic) calorimeters surrounding the outer detector sphere.

As a first step towards the realization of a detector of the above-mentioned type for LEP, we are currently elaborating the small drift chamber detector described in Section 4. The next step would be the realization of a larger counter with a photon detector area of the order of 0.5×0.5 m^2 and with a mirror of a diameter of about 1 m. Depending on the focal length of the mirror, such a counter could be made to subtend a substantial solid angle up to 1 sr as an element in the suggested LEP detector. Other developments

needed for the realization of this LEP detector concern the cryogenic system of the liquid neon counter. A prototype liquid neon radiation system and detector has been constructed at Saclay and will be tested later this year.

Acknowledgements

We would like to thank Dr. E. Gabathuler for his support of this research. Dr. J.M. Perreau provided the on-line programming capability, which was invaluable. Messrs. P. Queru and B. Goret were responsible for the construction of the detector. Mr. C. Detraz rendered technical assistance during all phases of the experiment and Mr. Y. Kornelis was responsible for the electronics. We express to all our appreciation for their contribution to this work.

References

1. Séguinot, J. and Ypsilantis, T., Nucl. Instrum. Methods 142, 377 (1977).

2. Gilmore, R.S., Malos, J., Bardsley, D.J., Lovett, F.A., Melot, J.P., Tapper, R.J., Giddings, D.I., Lintern, L., Morris, J.A.G., Sharp, P.H. and Wroath, P.D., Nucl. Instrum. Methods 157, 507 (1978).

3. Durkin, S., Homna, A. and Leith, E.W.G.S., Isabelle; Proc. 1978 Summer Workshop (BNL 50885, Brookhaven National Laboratory, Upton, New York, 1973). Also, SLAC-PUB 2186, August 1978.

4. Charpak, G., Majewski, S., Melchart, G., Sauli, F. and Ypsilantis, T., Nucl. Instrum. Methods 164, 419 (1979).

5. Comby, G., Mangeot, P., Auguères, J.L., Claudet, S., Chalot, J.F., Tichit, J., de Lignières, H. and Zadra, A., Saclay Report 79/06/08/227 (1979).

6. Séguinot, J., Tocqueville, J. and Ypsilantis, T., Imaging Čerenkov detector: photoionization of triethylamine, preprint CERN-EP/79-161 (1979), submitted to Nucl. Instrum. Methods.

7. Charpak, G. and Sauli, F., Phys. Lett. 78B, 523 (1978).

8. Nakato, Y., Ozaki, M. and Tsubomura, I., Bull. Chem. Soc. Japan 45, 1299 (1972) and 47, 3001 (1974).

9. Cetinkaya, B., King, G.H., Krishnamurthy, S.S., Lappert, M.F. and Pedley, J.B., Chem. Commum., p. 1370 (1971).

10. Ekelöf, T., Possibilities and limitations of the Čerenkov ring-imaging technique at very high energies, Proc. ICFA Workshop, Les Diablerets, 1979 [editor, U. Amaldi, CERN, Geneva (in press)].

Figure captions

Fig. 1 : Experimental layout showing argon radiator gas cylinder, mirror, detector, and trigger scintillators.

Fig. 2 : Detector construction and dimensions.

Fig. 3 : a) Preamplification gap gain and transfer efficiency G_{PA} versus potential difference across the PA gap.
b) Proportional chamber gain G_{PC} versus potential difference between cathode and wires.

Fig. 4 : a) Single photoelectron counts per incident pion (n_{pe}) versus potential difference across the PA gap.
b) Single photoelectron counts per incident pion (n_{pe}) versus potential difference in the proportional chamber.

Fig. 5 : a) The number of events $N(n_w)$ having n_w hit wires per incident pion for a sample of 10^4 pions (10 GeV/c).
b) The number of events $N(n_{pe})$ having n_{pe} photoelectrons per incident pion for a sample of 10^4 pions (10 GeV/c).

Fig. 6 : The number of photoelectrons $n_{pe}(x)$ versus wire position x for $M = 10^4$ incident 10 GeV/c pions (data points are with error bars). The histogram is the best fit of $n\bar{MP}_i$ to the data points with fit values $n = 2.85$, $r = 26.04$ mm, $x_c = -6.59$ mm, and $\alpha = \pm 2.5$ mrad.

Fig. 7 : Correction curve which relates the observed average number of photoelectrons per event n versus the true assumed number N obtained by a Monte Carlo simulation with the parameters $r = 27$ mm, $x_c = -6$ mm, and $\alpha = \pm 1.25$ mm for the three indicated values of the smearing probability.

Fig. 8 : The measured 5 mm thick CaF_2 crystal transmission T, and the measured mirror reflectivity R, with the relative TEA quantum efficiency Q/Q_{max} all versus photon energy E. The product of these three curves is labelled total.

Fig. 9 : The argon + methane + TEA single photoelectron counts (n_{pe}) per incident 10 GeV/c pion versus the proportional chamber applied potential V_{pc}. The dotted curve at level $n_{pe} = 3$ is the count rate observed without methane, and the dotted curves labelled $E_2 = 8.7$ eV and $E_2 =$ $= 8.6$ eV is the count rate expected if all photons of energy above E_2 are absorbed in methane rather than in TEA.

Fig. 10 : The relative quantum efficiency Q/Q_{max} of TEA with the methane absorption probability versus photon energy E.

Fig. 11 : Schematic view of a drift chamber for detection of the ring image.

Fig. 12 : Prototype drift detector.

Fig. 13 : The measured transmission of an 8 mm thick fused quartz window, and the relative quantum efficiencies (normalized to 50% at E = 7.2 eV) of TMBI and TMAE versus photon energy E.

Fig. 14 : In this linear plot the left curve shows how the normalized Čerenkov angle $\theta_n = \theta/\theta_{max}$ grows from zero at the normalized velocity $\gamma_n = 1$ up towards the maximum value 1 at large velocities. Taking the ordinate to be a relative energy scale normalized to the threshold energy for pions, the three curves correspond to π, K, and p as indicated. The ordinate on the right-hand side shows the normalized number of emitted Čerenkov photons.

Fig. 15 : log-log plot of $(1-\theta_n)$ versus E_n showing in detail how the three curves in Fig. 14 approach their asymptote.

Fig. 16 : A dodecahedron detector structure surrounding the LEP interaction region is composed of 12 pentagons. Each pentagon is subdivided into five triangular drift regions with proportional wires on the periphery. More detail is shown in the following figure.

Fig. 17 : The liquid-neon radiator and detector system which is composed of 12 such elements, each having an angular acceptance of $\pi/3$ sr. This cryogenic element may be followed by a STP xenon gas radiator and detector system.

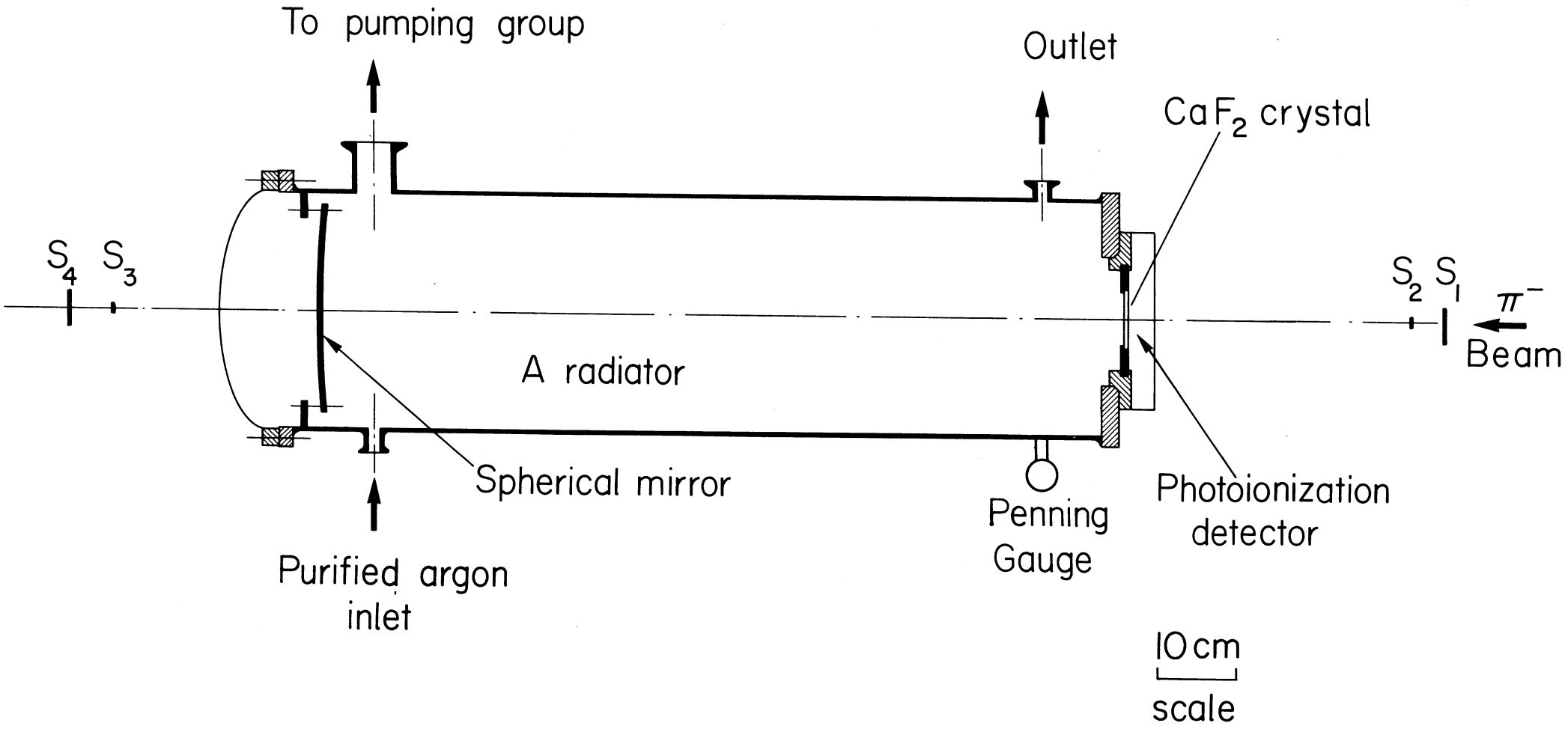
To pumping group
Outlet
CaF2 crystal
S4
S3
S2
S1
π−
Beam
A radiator
Spherical mirror
Penning Gauge
Photoionization detector
Purified argon inlet
10 cm
scale

Fig. 1

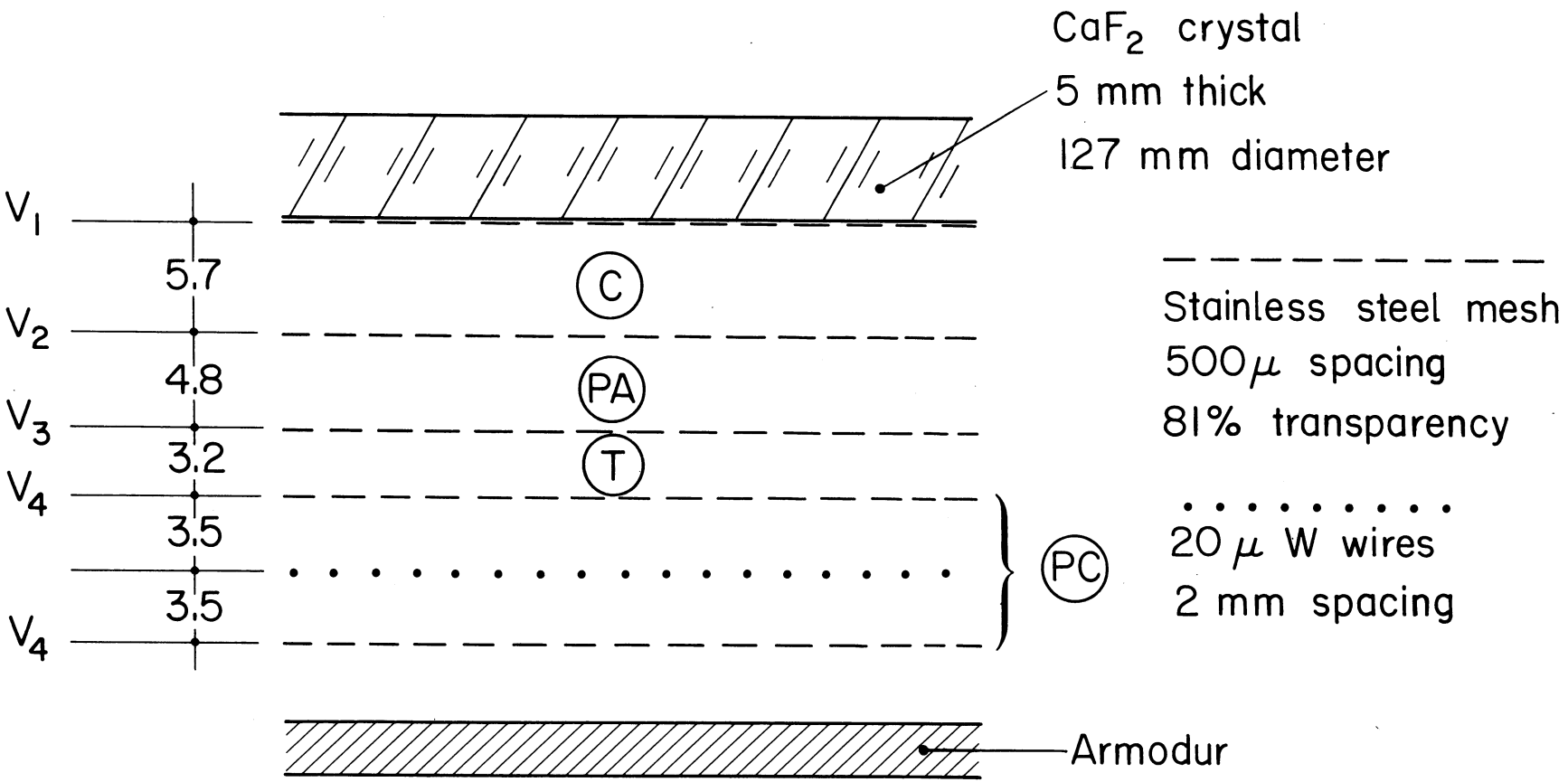
CaF2 crystal
5 mm thick
127 mm diameter
V1
5.7
V2
C
4.8
V3
PA
3.2
V4
T
3.5
3.5
V4
PC
Stainless steel mesh
500μ spacing
81% transparency
20μ W wires
2 mm spacing
Armodur

Fig. 2

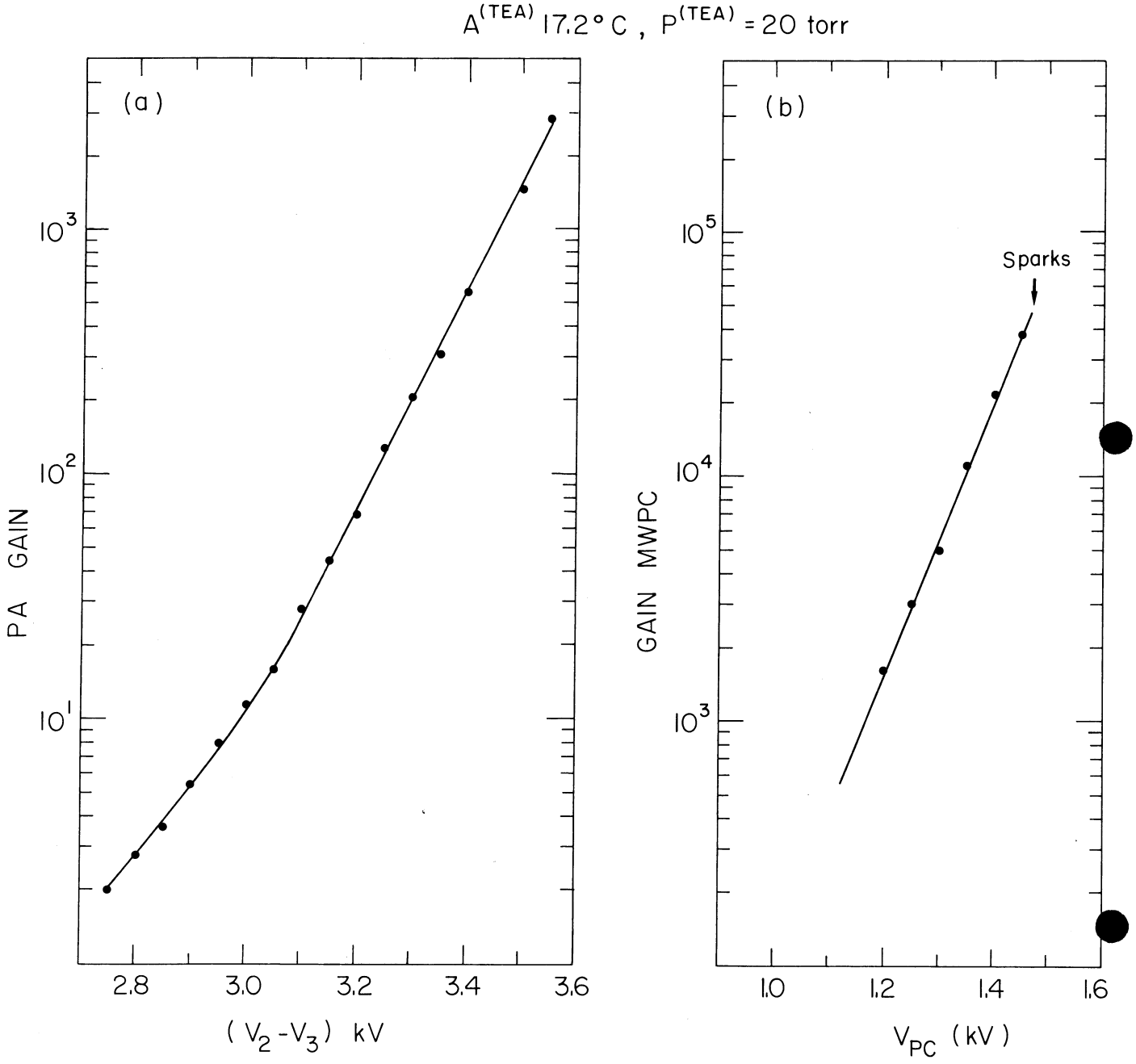
A(TEA) 17.2° C , P(TEA) = 20 torr
(a)
PA GAIN
10^3
10^2
10^1
2.8
3.0
3.2
3.4
3.6
(V2 - V3) kV
(b)
GAIN MWPC
10^5
10^4
10^3
Sparks
1.0
1.2
1.4
1.6
VPC (kV)

Fig. 3

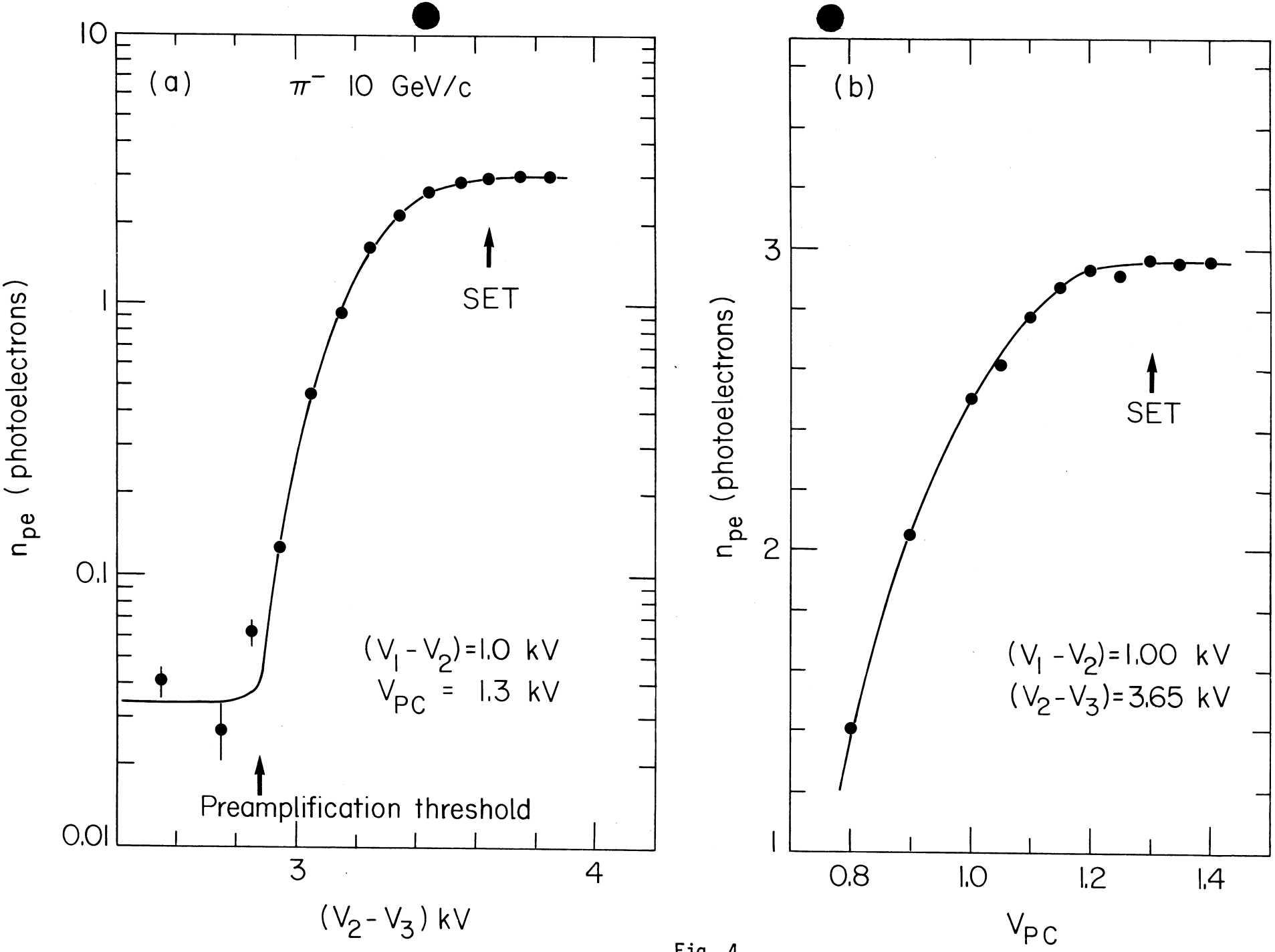
(a)
π^- 10 GeV/c
SET
$(V_1 - V_2) = 1.0$ kV
V_{PC} = 1.3 kV
Preamplification threshold
n_{pe} (photoelectrons)
$(V_2 - V_3)$ kV
10
1
0.1
0.01
3
4
(b)
SET
$(V_1 - V_2) = 1.00$ kV
$(V_2 - V_3) = 3.65$ kV
n_{pe} (photoelectrons)
V_{PC}
3
2
1
0.8
1.0
1.2
1.4

Fig. 4

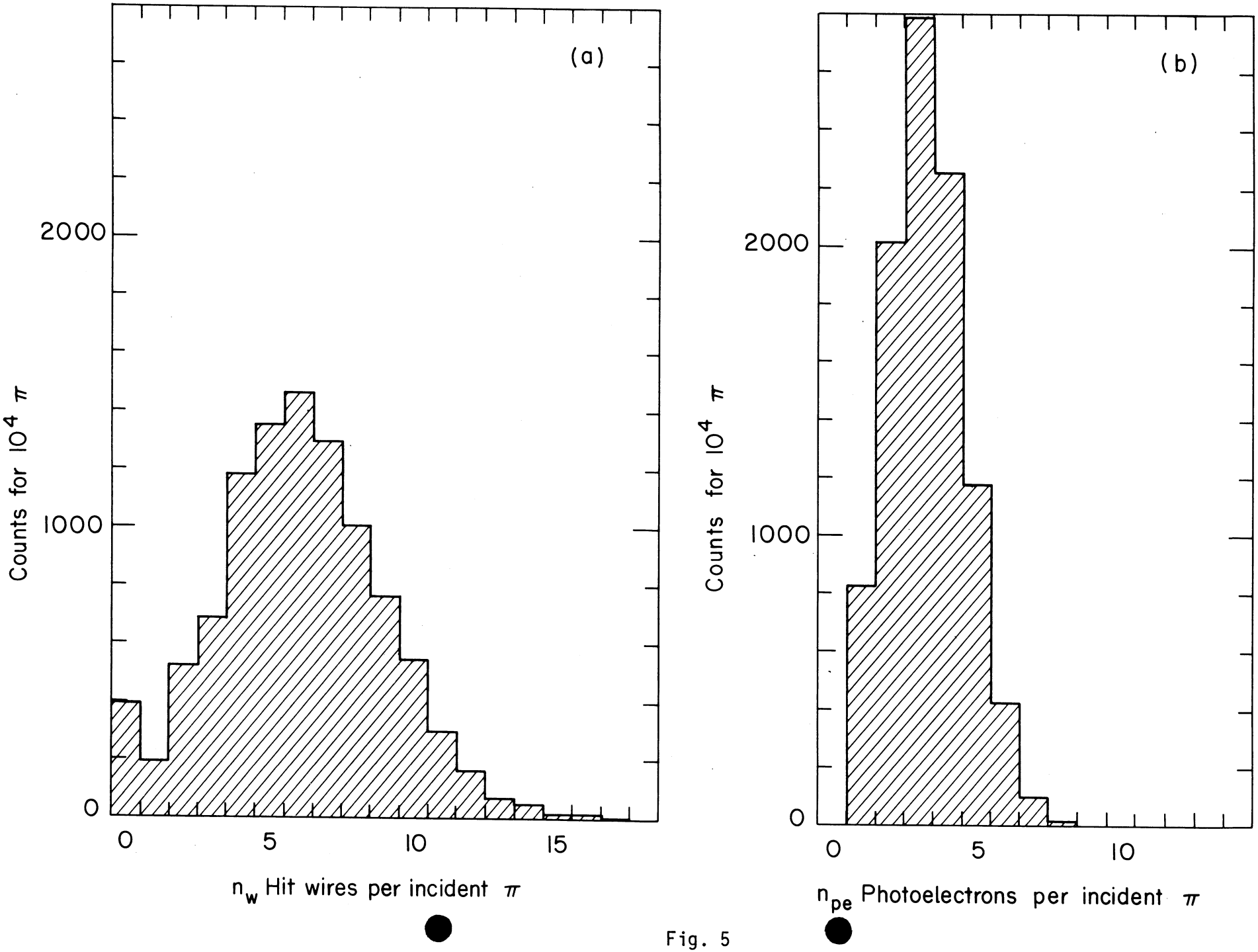
(a)
2000
1000
0
Counts for 10^4 π
0
5
10
15
n_w Hit wires per incident π
(b)
2000
1000
0
Counts for 10^4 π
0
5
10
n_{pe} Photoelectrons per incident π

Fig. 5

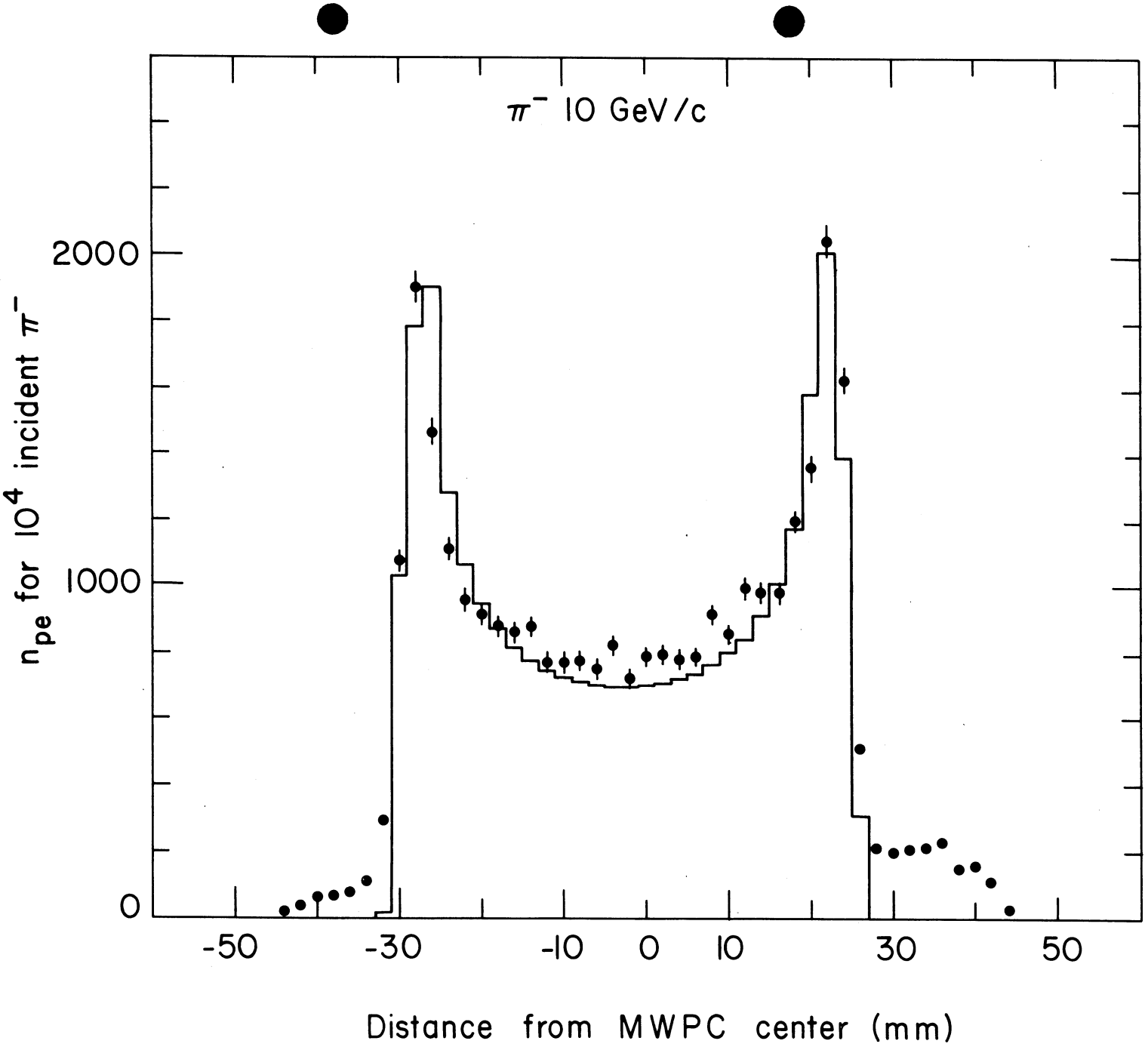
π^- 10 GeV/c
2000
1000
0
n_{pe} for 10^4 incident π^-
-50
-30
-10
0
10
30
50
Distance from MWPC center (mm)

Fig. 6

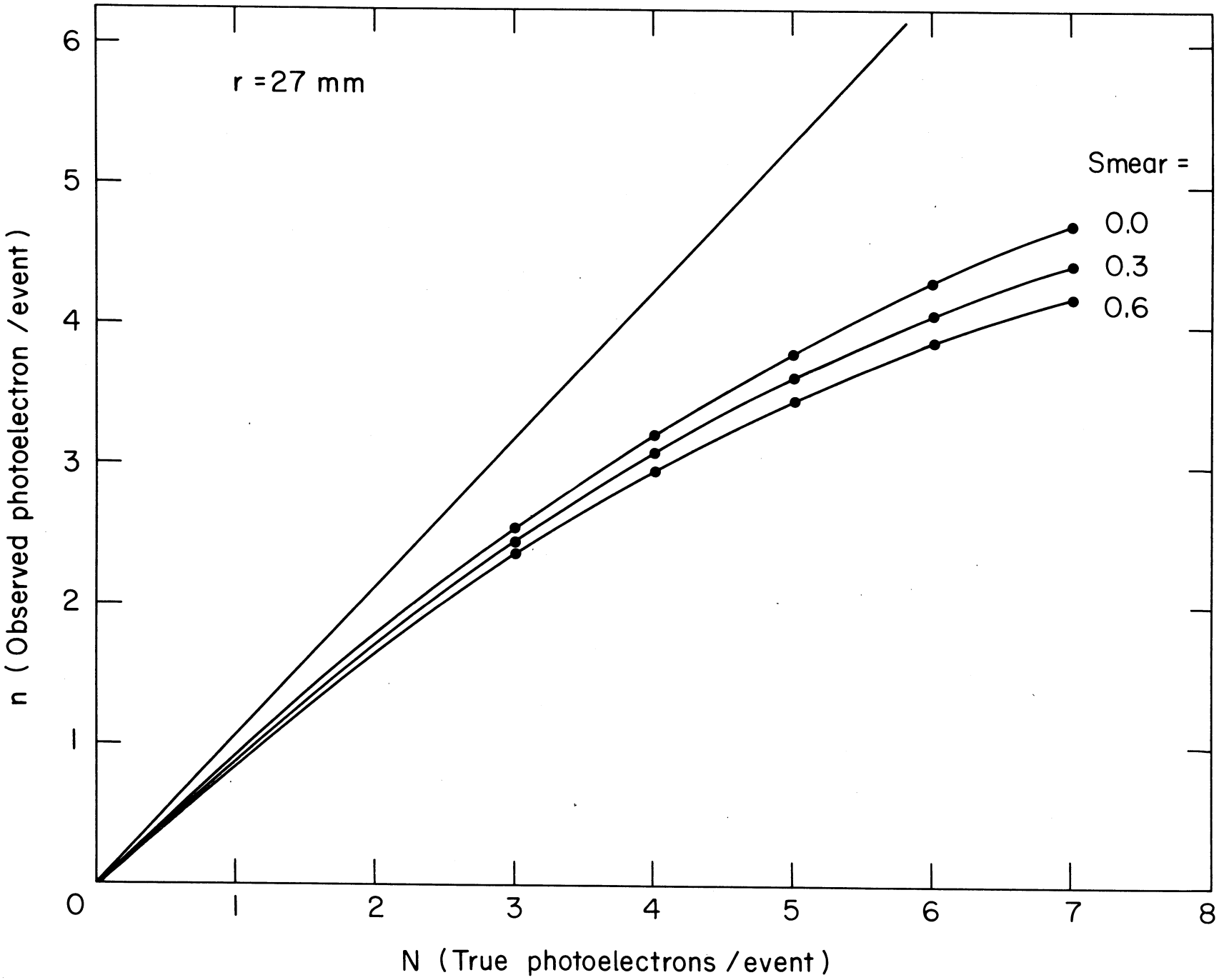
r =27 mm
Smear =
0.0
0.3
0.6
n (Observed photoelectron /event)
N (True photoelectrons / event)
0
1
2
3
4
5
6
7
8

Fig. 7

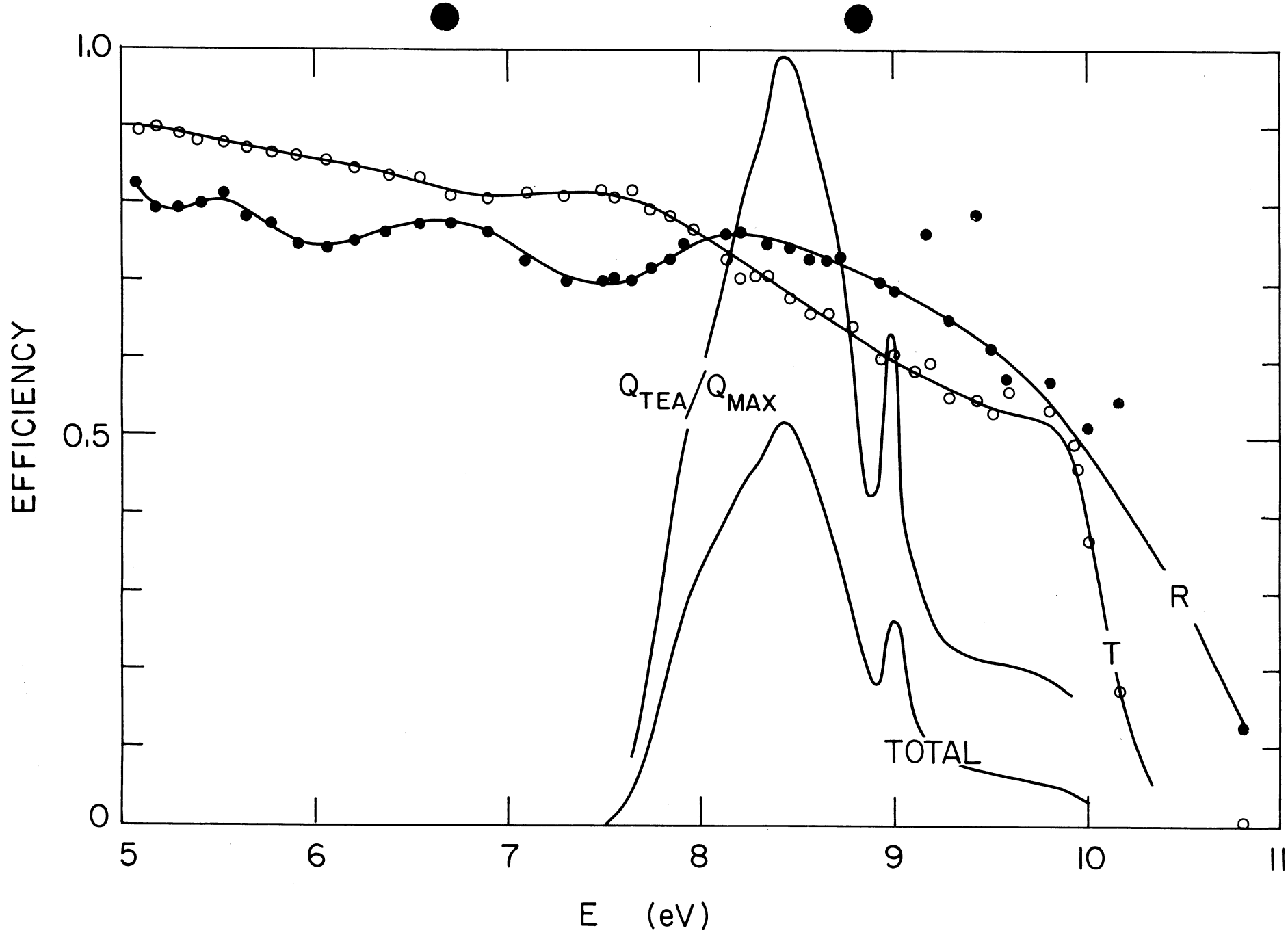

Fig. 8

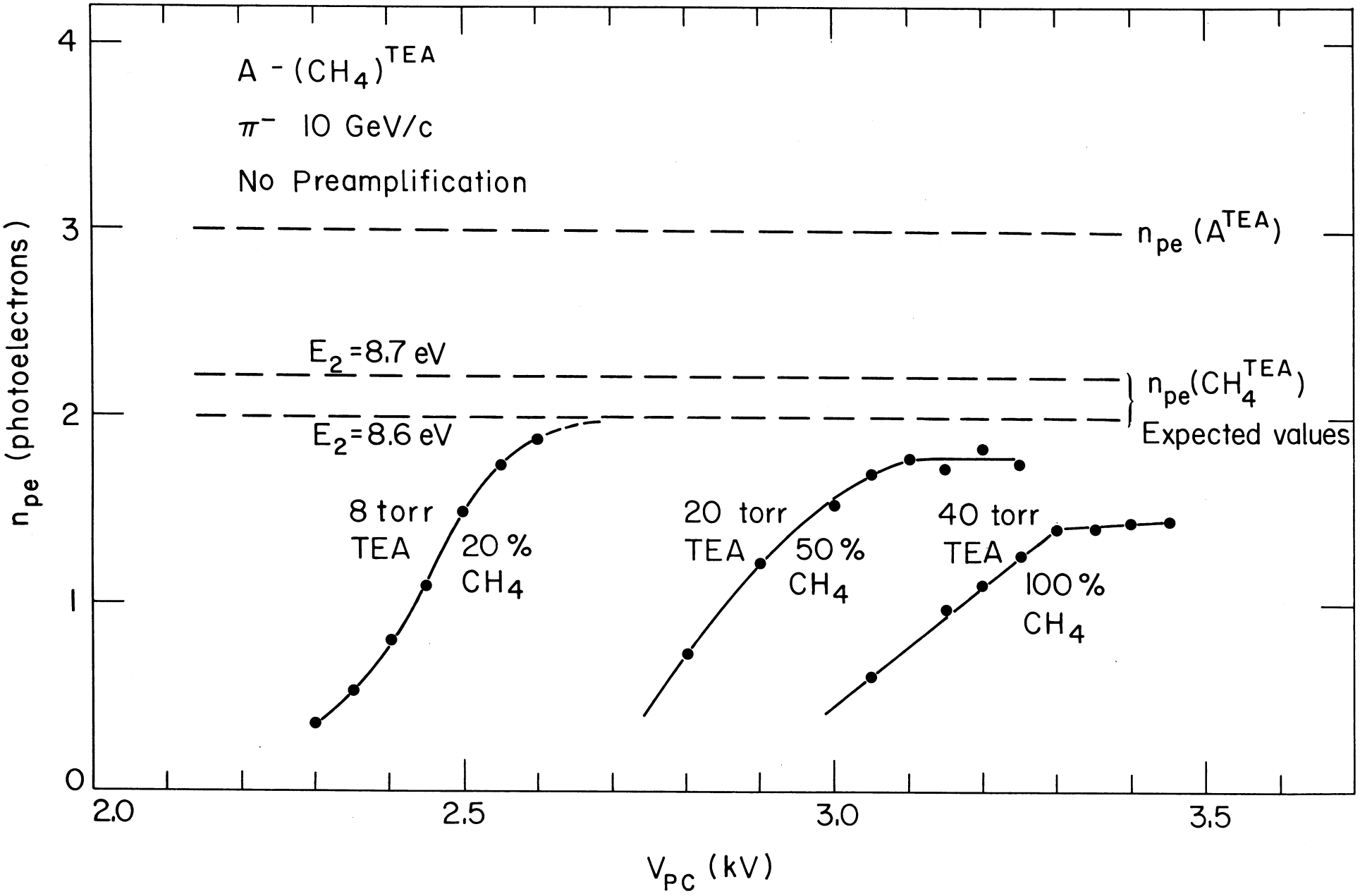
A - $(CH_4)^{TEA}$
π^- 10 GeV/c
No Preamplification
n_{pe} (A^{TEA})
E_2 = 8.7 eV
E_2 = 8.6 eV
$n_{pe}(CH_4^{TEA})$
Expected values
8 torr TEA
20 % CH_4
20 torr TEA
50 % CH_4
40 torr TEA
100 % CH_4
n_{pe} (photoelectrons)
V_{PC} (kV)
0
1
2
3
4
2.0
2.5
3.0
3.5

Fig. 9

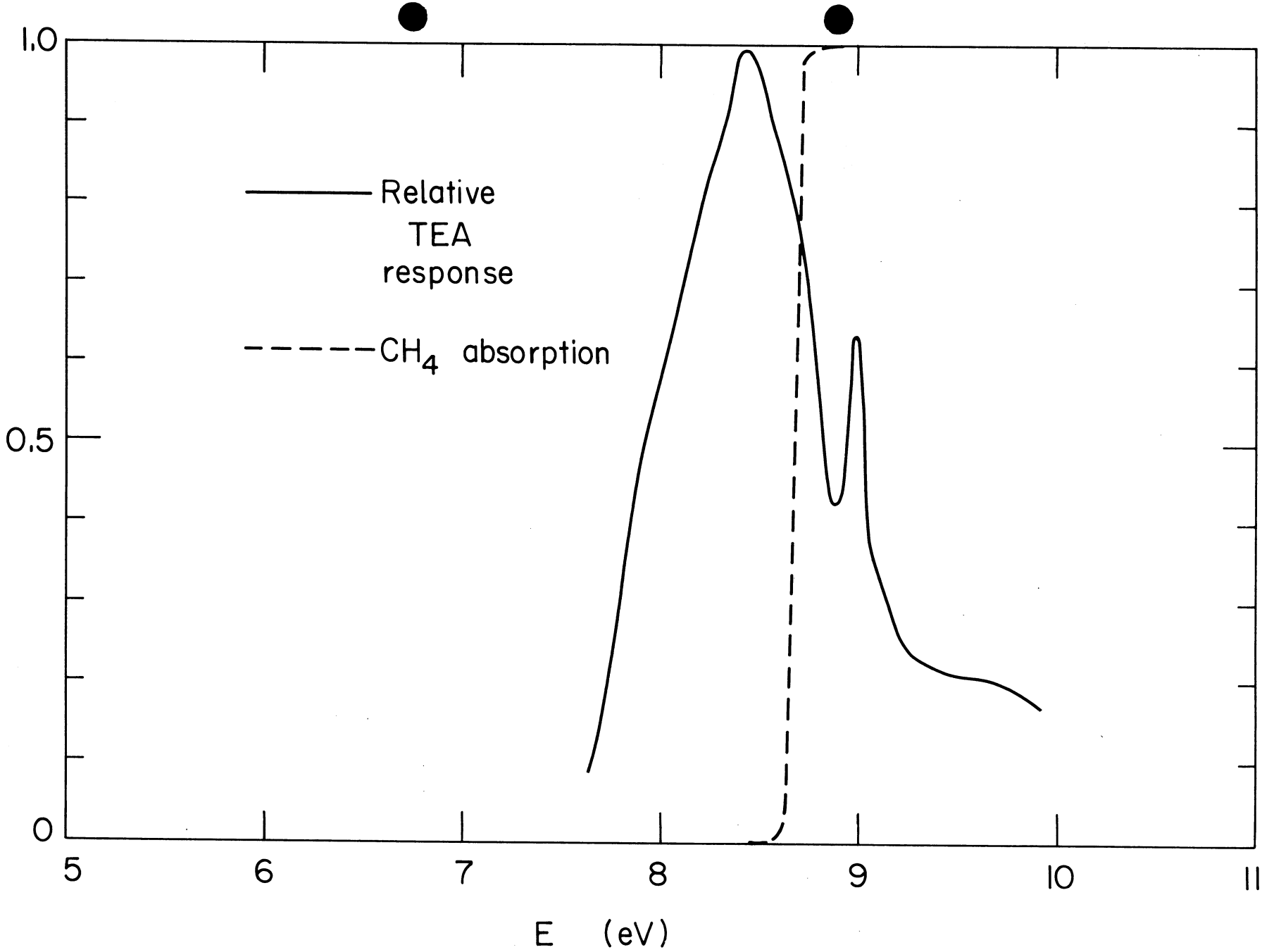

Fig. 10

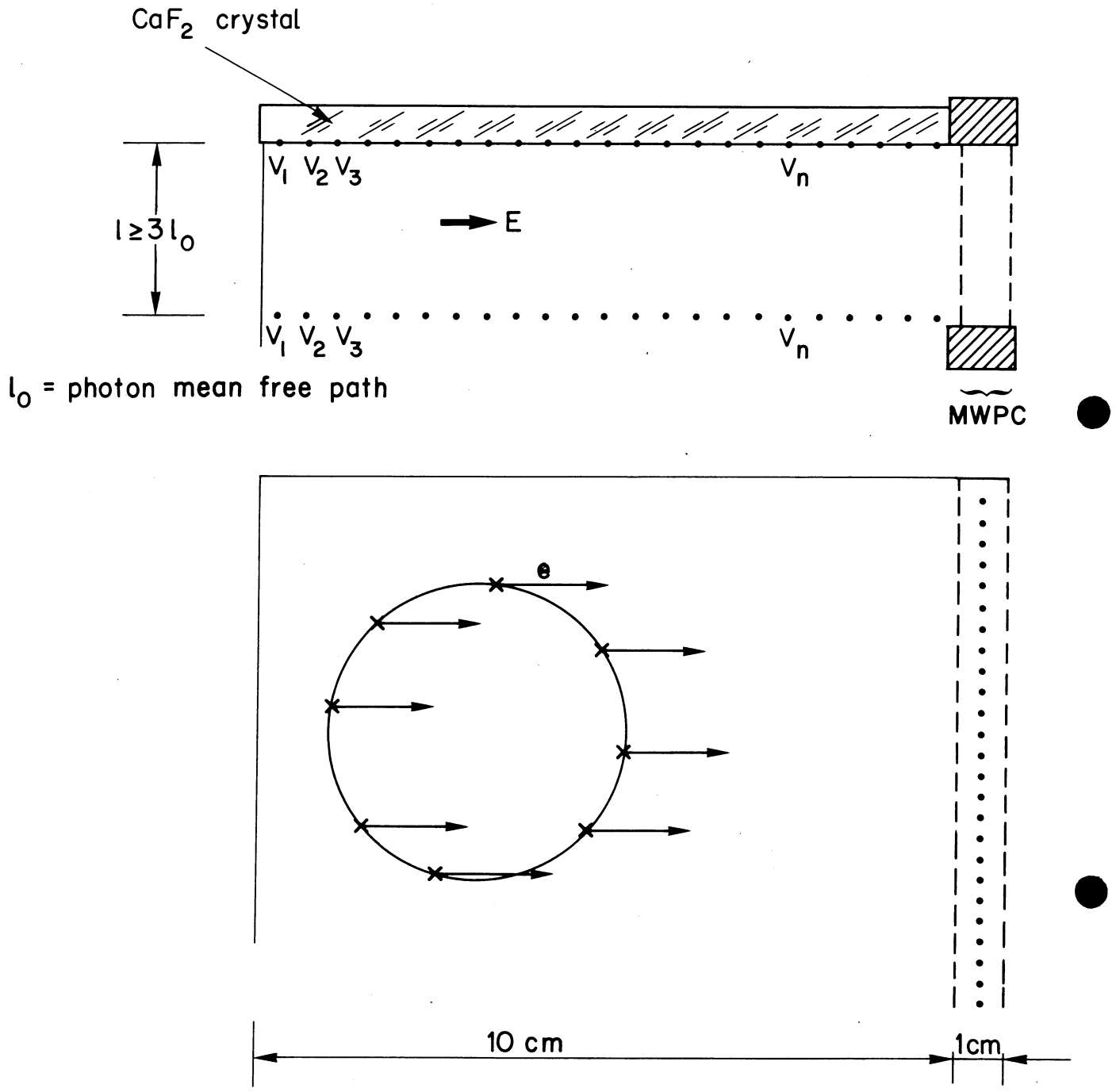
CaF2 crystal
V1 V2 V3
Vn
E
l ≥ 3 l0
V1 V2 V3
Vn
l0 = photon mean free path
MWPC
e
10 cm
1cm

Fig. 11

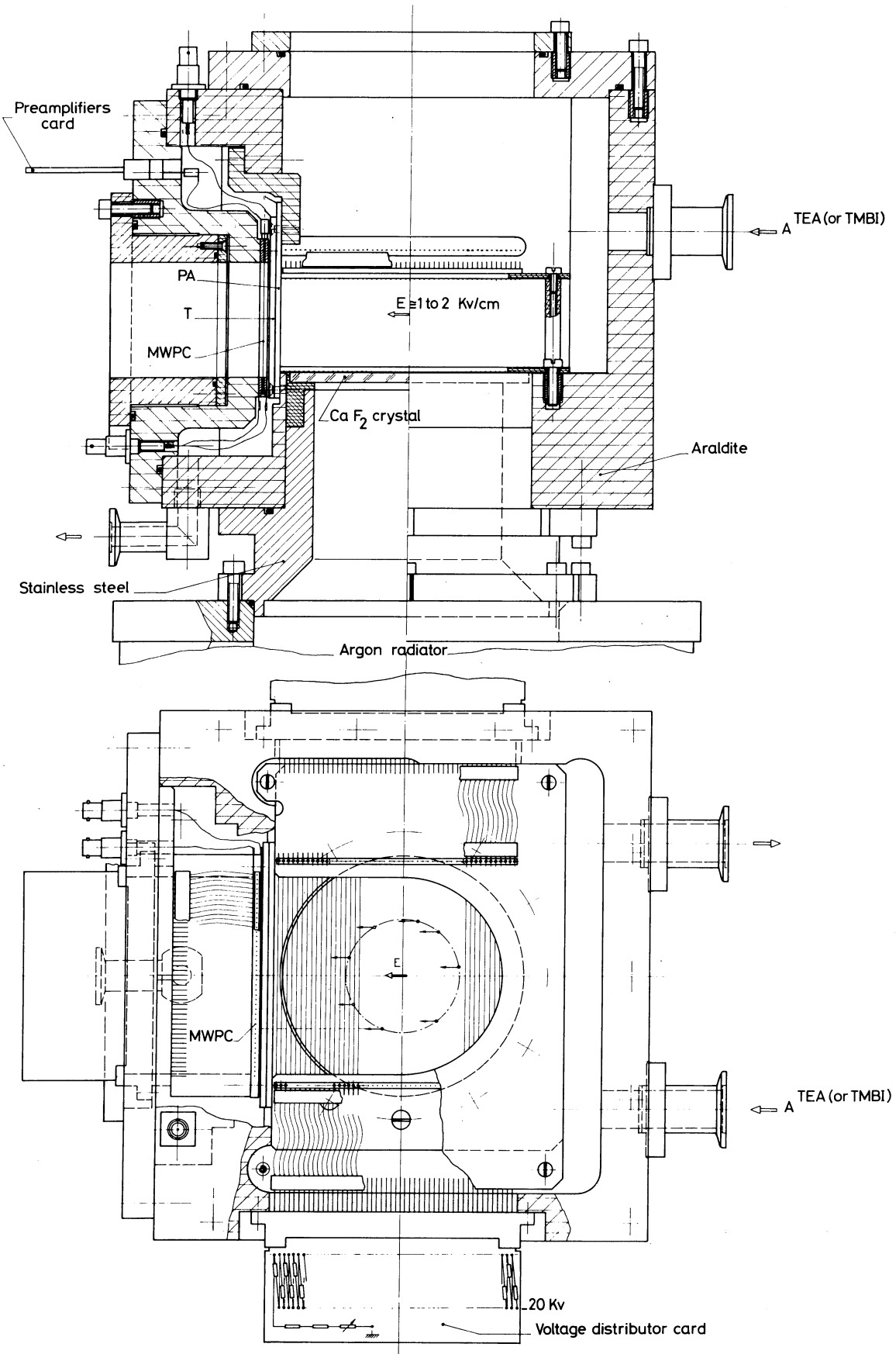

RING IMAGING TPC DETECTOR
EXPERIMENTAL CHAMBER

Fig. 12

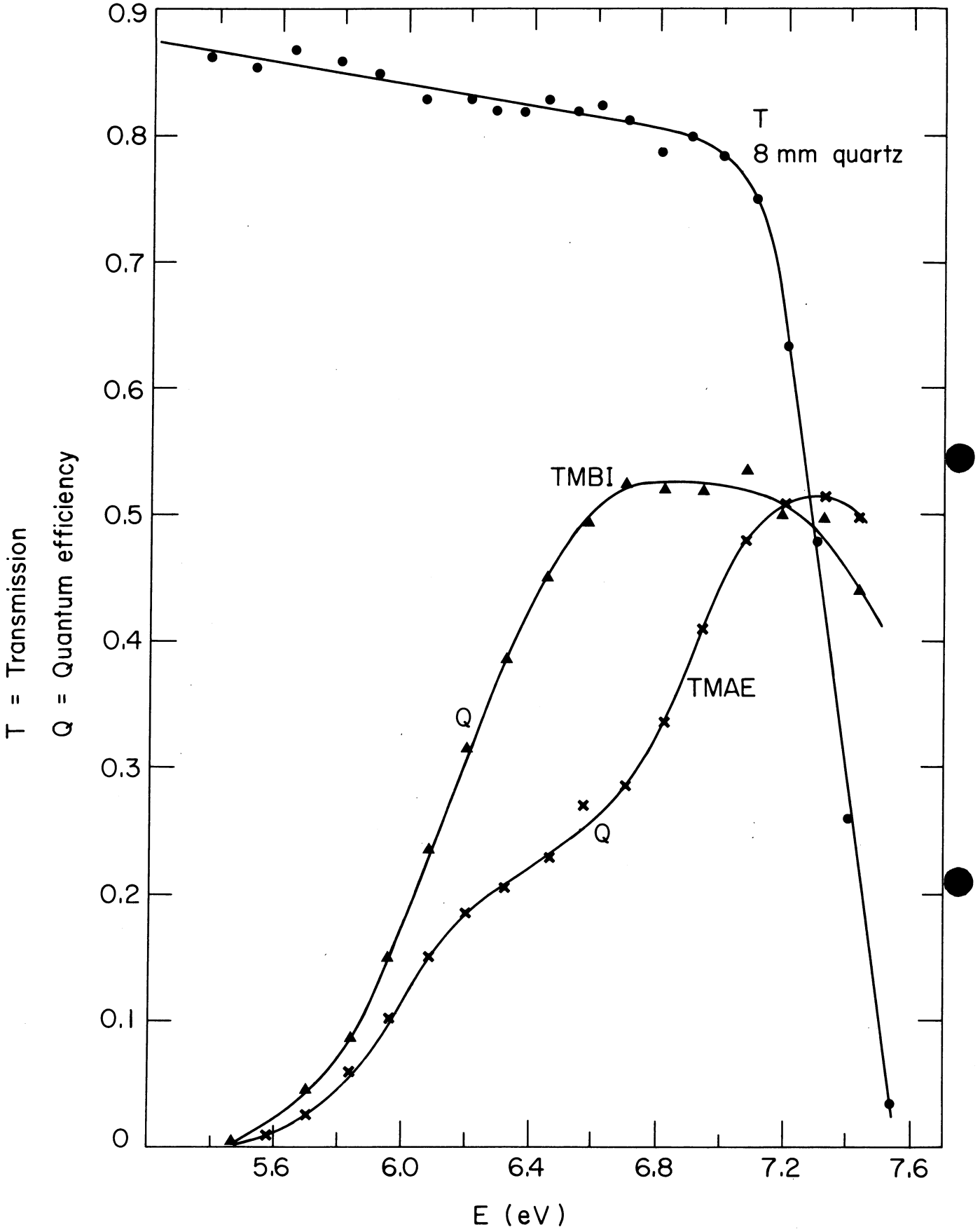
T = Transmission
Q = Quantum efficiency
0.9
0.8
0.7
0.6
0.5
0.4
0.3
0.2
0.1
0
5.6
6.0
6.4
6.8
7.2
7.6
E (eV)
T
8 mm quartz
TMBI
Q
TMAE
Q

Fig. 13

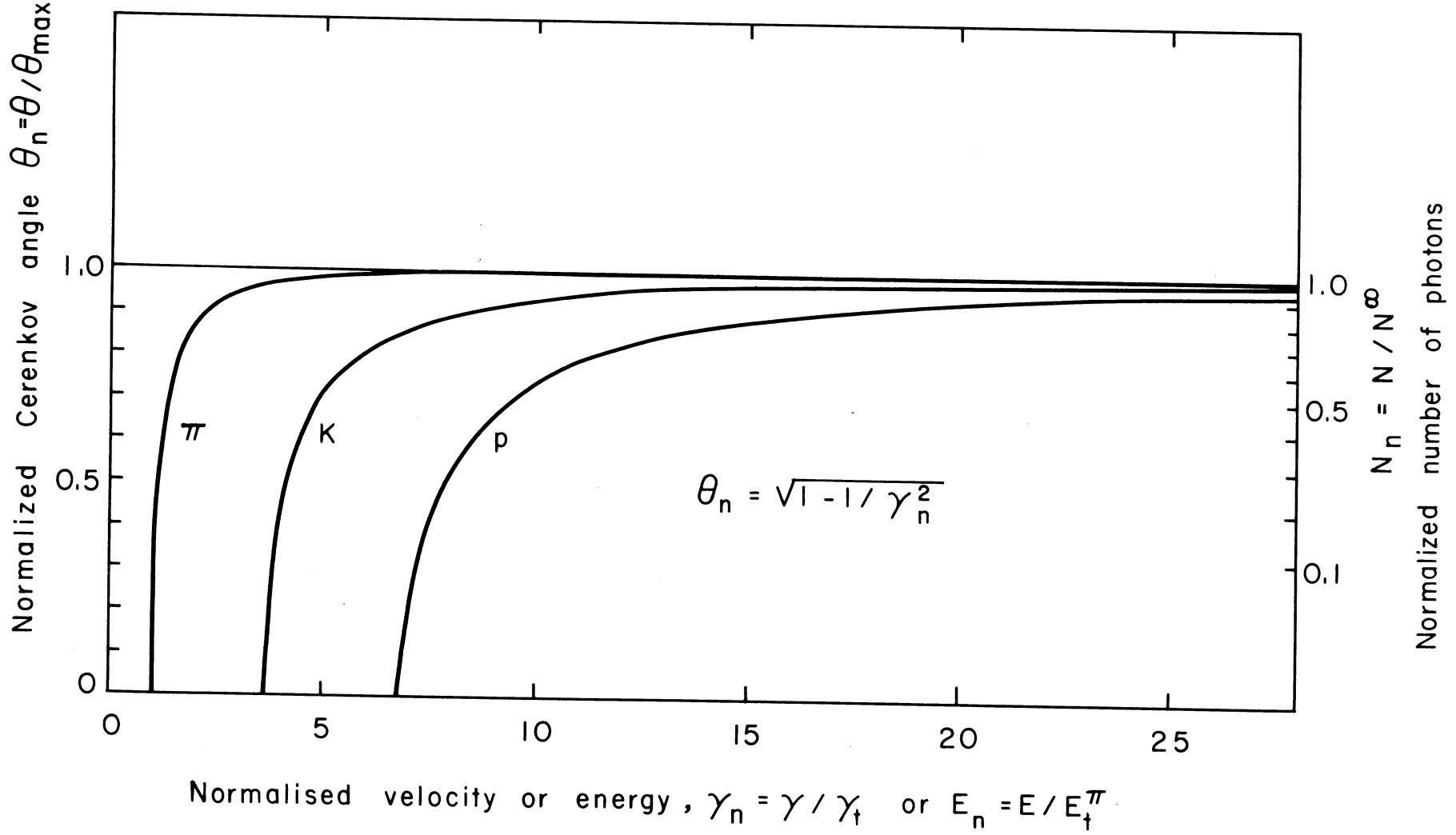
Normalized Cerenkov angle $\theta_n = \theta / \theta_{max}$
1.0
0.5
0
π
K
p
$\theta_n = \sqrt{1 - 1/\gamma_n^2}$
0
5
10
15
20
25
Normalised velocity or energy, $\gamma_n = \gamma / \gamma_t$ or $E_n = E / E_t^{\pi}$
1.0
0.5
0.1
$N_n = N / N^{\infty}$
Normalized number of photons

Fig. 14

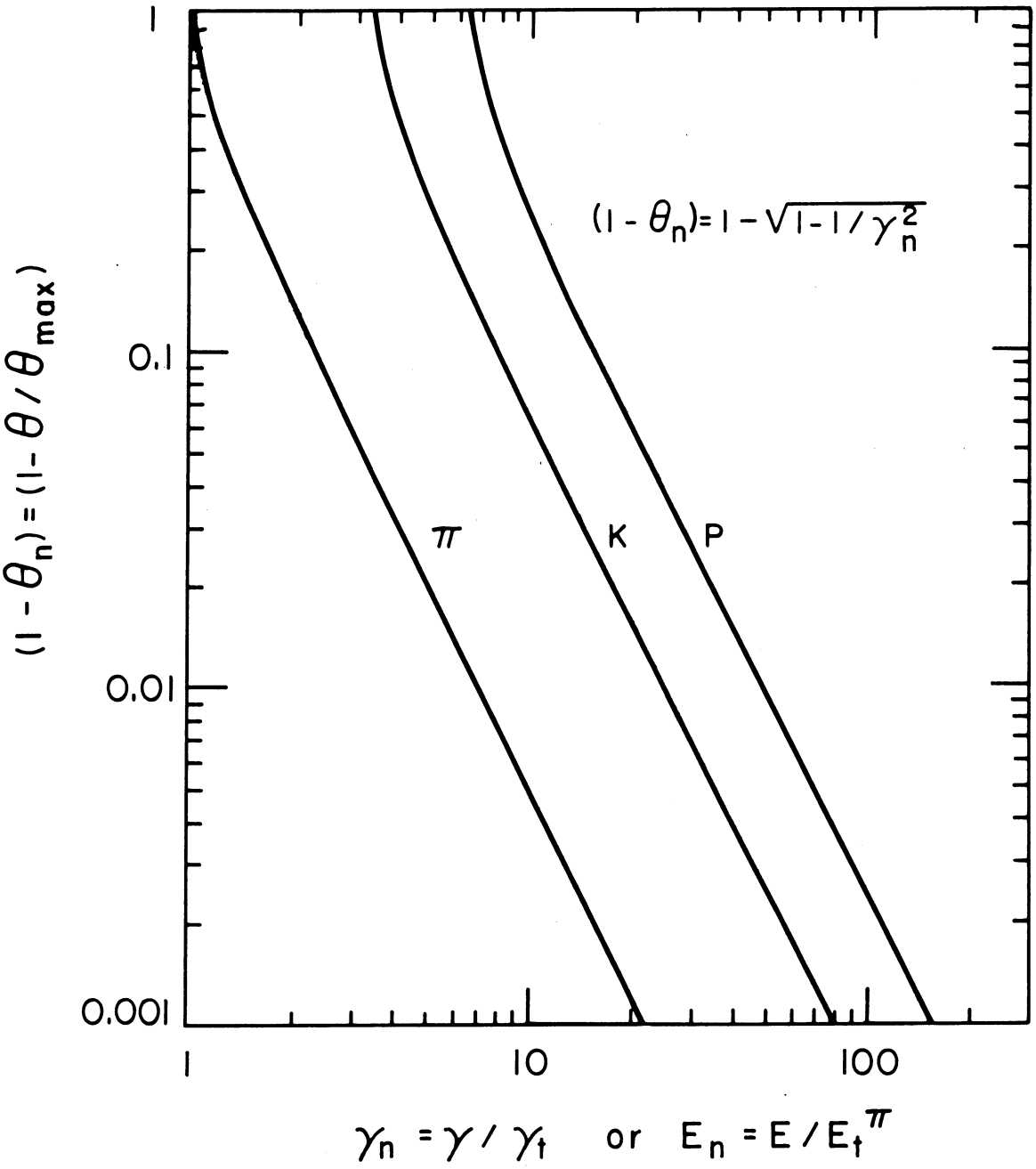
1
0.1
0.01
0.001
1
10
100
$(1-\theta_n)=1-\sqrt{1-1/\gamma_n^2}$
π
K
P
$(1-\theta_n)=(1-\theta/\theta_{max})$
$\gamma_n=\gamma/\gamma_t$ or $E_n=E/E_t^{\pi}$

Fig. 15

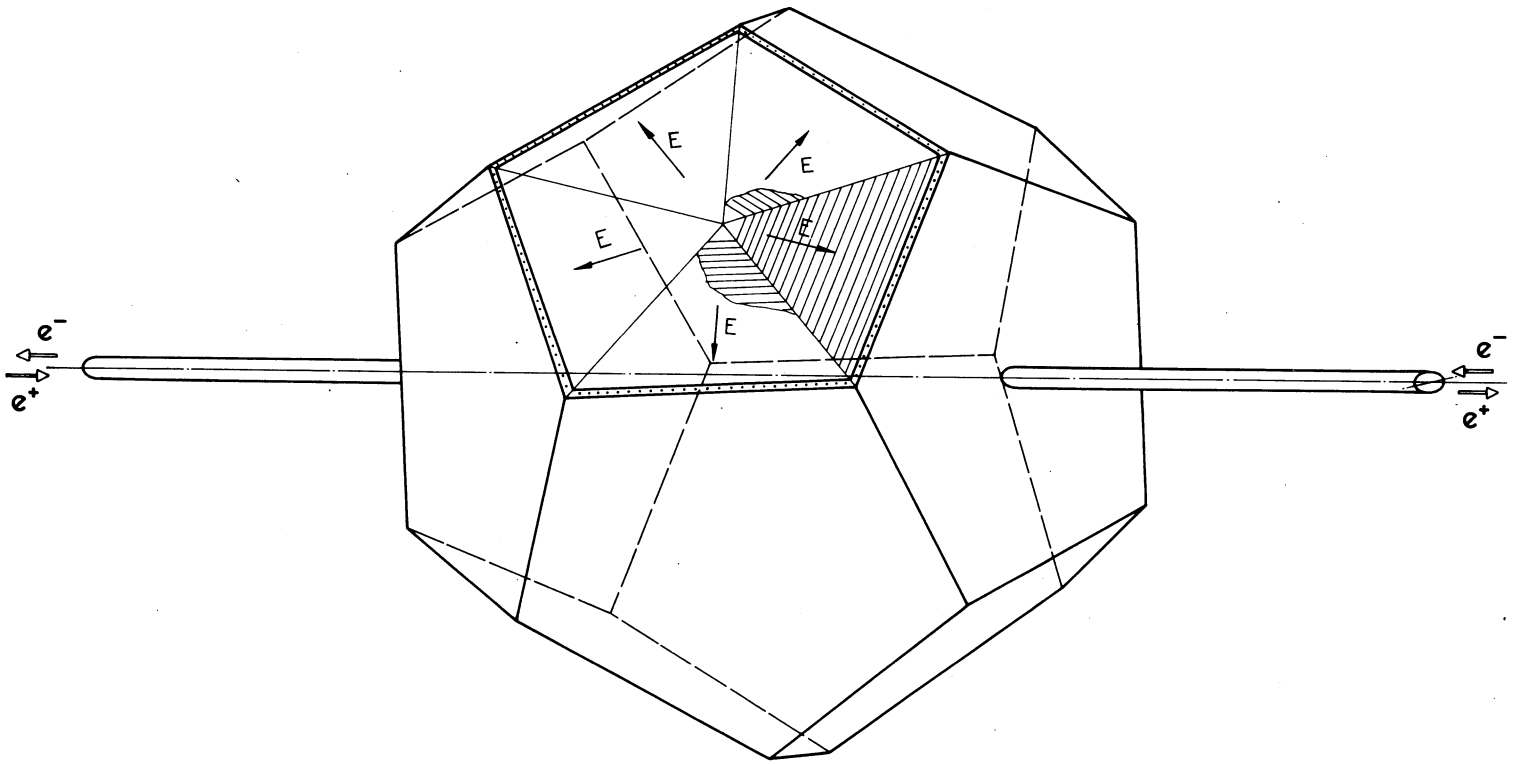

LEP DETECTOR STUDY

Fig. 16

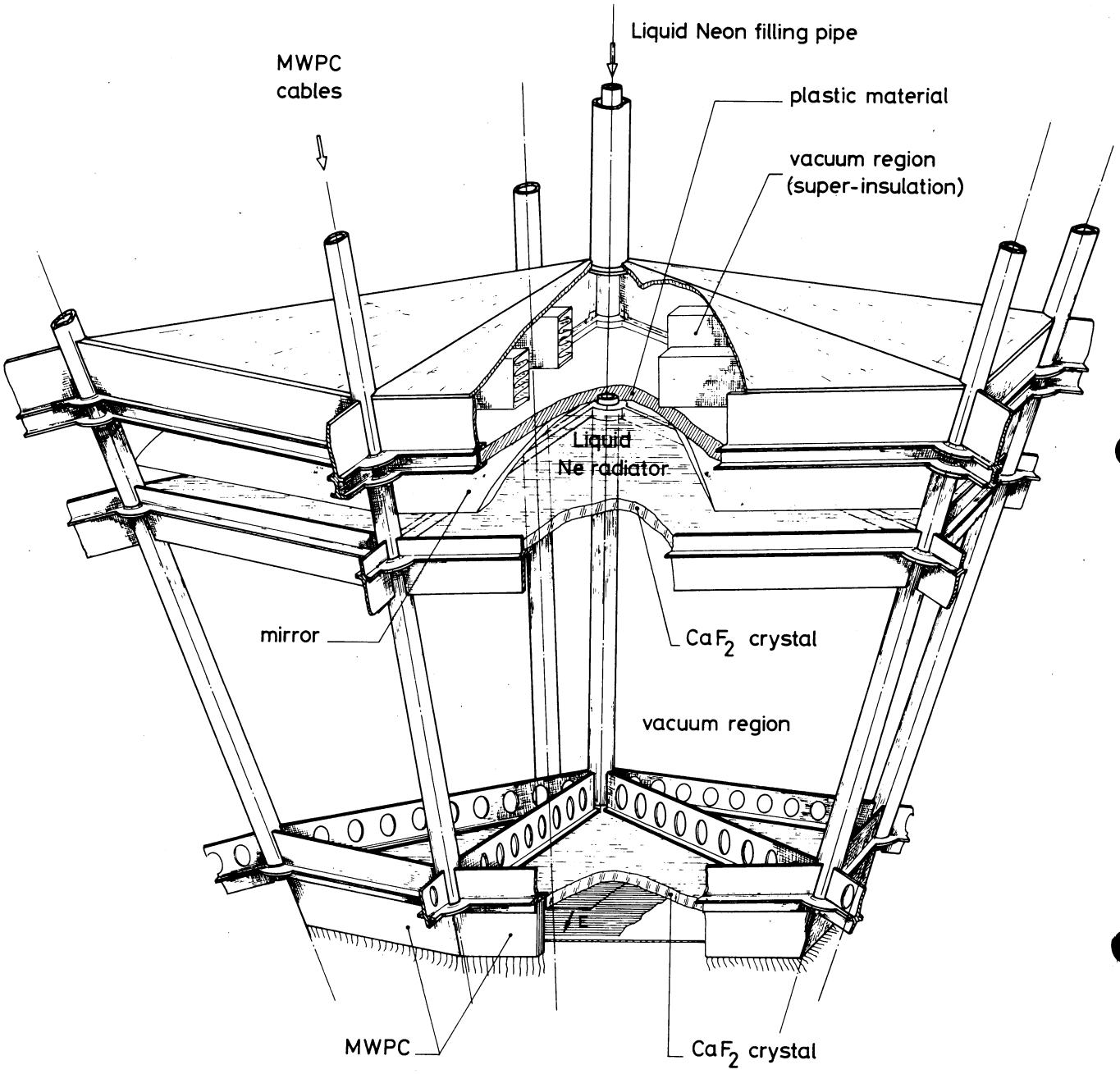

LEP DETECTOR STUDY

Fig. 17